Shape Optimization of Vortex Generators to Control Mack Mode Amplification

Clark C. Pederson*
The University of Texas at Austin, Austin, TX, 78712, USA

Meelan M. Choudhari†
NASA Langley Research Center, Hampton, VA, 23681, USA

Beckett Y. Zhou‡
Chair for Scientific Computing, TU Kaiserslautern,
Bldg 34, Paul-Ehrlich-Strausse, 67663 Kaiserslautern, Germany

Pedro Paredes§, Boris Diskin¶
National Institute of Aerospace (NIA), Hampton, VA, 23681, USA

This paper demonstrates the potential to use shape optimization for the design of vortex generators in an axisymmetric boundary layer. This shape optimization increases the amplitude of stationary streaks created by streamwise vorticity, with the goal of reducing the amplification of Mack mode instabilities. The test case under consideration matches a trajectory point during the ascent phase of the HIFiRE-1 flight experiment. Wall-mounted vortex generators are added to the cone and their shape is optimized to control the amplification of Mack mode instabilities that are known to initiate laminar-turbulent transition in this flow. An empirical objective function is developed based on the previous studies of optimal streaks. A constraint on the maximum streak amplitude is added to avoid the initiation of bypass transition. The shape optimization is conducted using SU2, an open-source suite for multiphysics simulation and design. A significant improvement is observed in an integral metric of the streak amplitude, while the maximum streak amplitude is maintained close to the baseline level. The qualitative features of the optimized geometry are discussed.

Nomenclature

k	=	vortex generator height, measured from the cone surface
t	=	time
u	=	streamwise velocity
(x, y, z)	=	Cartesian coordinate system
A	=	streak amplitude
C	=	inequality constraint
J	=	objective function
L^*	=	reference lengthscale [m]
L_c^*	=	length of the cone [m]
$\mathcal{L}$	=	Lagrangian
M	=	Mach number
$\mathcal{M}$	=	mesh deformation, mapping the design variables to the discrete mesh
N	=	number of grid points in a given direction
R	=	residual of the compressible Navier-Stokes equation

*Graduate Student, Walker Department of Mechanical Engineering, The University of Texas at Austin, AIAA Student Member
†Aerospace Technologist, Computational AeroSciences Branch. AIAA Fellow
‡Research Scientist, AIAA Member
§Research Engineer, Computational AeroSciences Branch, Senior Member AIAA
¶NIA Research Fellow, AIAA Associate Fellow

Re = unit Reynolds number [m^{-1}]
T^* = temperature [K]
U = state vector for the direct solution
X = vector representing the discretized mesh
α = vector of design variables
δ_h^* = boundary layer thickness, measured at $x^* = 0.6$m [m]
(ξ, η, ζ) = streamwise, wall-normal, and azimuthal coordinates [m, m, -]

Superscripts

$\bar{\cdot}$ = adjoint flow solution
$*$ = dimensional value

Subscripts

∞ = freestream conditions

I. Introduction

Hypersonic vehicles are subject to strong aerodynamic heating and skin friction, both of which increase substantially after the boundary layer transitions to turbulence. Therefore, to reduce the heat load and the vehicle drag, the laminar region of the boundary layer should extend as far as possible. This motivates the study of the laminar-turbulent boundary layer transition in hypersonic flows.

Transition to turbulence can happen through several mechanisms. One mechanism is contamination through either strong freestream disturbances or surface roughness. If these background disturbances are minimal, then transition occurs due to the exponential amplification of modal instabilities. The nature of the modal instabilities depends on the freestream Mach number. In the incompressible regime, the most amplified disturbances are planar two-dimensional Tollmien-Schlichting waves. In the hypersonic regime and in the absence of strong crossflow effects or regions of concave surface curvature, second modes, also known as Mack modes, dominate transition [1]. Bypass transition can occur if a large disturbance is introduced to an otherwise stable boundary layer.

Often, roughness elements or vortex generators are used to trigger bypass transition. Nevertheless, research has shown that moderately sized roughness elements or vortex generators can actually improve the stability of the boundary layer. Disturbances of a proper amplitude and wavelength can destructively interfere with the most unstable modes, damping their amplification rates. James [2] studied two-dimensional roughness elements in a boundary layer with a freestream Mach number between 2.8 and 7. He found that the wall roughness could delay transition, and that there existed an optimum height that led to the largest delay in transition. Fong et al. [3, 4] conducted numerical and experimental studies to investigate the effect of two-dimensional roughness elements on hypersonic boundary layers at M=6. Both experiments and numerical simulations confirmed that properly placed roughness elements could suppress the dominant Mack modes. Research by Paredes et al. [5–7] confirmed that streaks of streamwise vorticity can also reduce the growth of second mode disturbances and showed [7] that optimal streaks can extend the length of the laminar region by more than 100%.

Multiple studies have examined the interaction between Mack modes and stationary streaks created by streamwise vortices. Paredes et al. [8] examined a Mach 3 flat-plate boundary layer and confirmed that stationary streaks reduced the amplification rate of Mack mode instabilities. A similar stabilization effect was found in an axisymmetric boundary layer at a Mach number of 5.3 [7]. This second study showed that the planar Mack mode still dominated the instability, even after the introduction of stationary streaks. By damping the growth of these dominant modes, transition was effectively delayed for both cases.

Recent transition research has focused on small bumps that generate vortices or streamwise streaks, which we will refer to as vortex generators. There are many geometrical parameters that influence the streamwise streaks. These parameters include their height and slope, the azimuthal or spanwise spacing, and the streamwise spacing. In the initial research exploring the application of roughness elements or vortex generators for controlling the growth of unstable disturbances, designs often favored simplicity. For example, spherical bumps [9] or screw-like threads [2] were used. The relationship between the transition delay and the vortex generator shape is still a research topic.

Several studies have tried to fill this gap in the research. Paredes et al. [6–8] utilized optimal growth theory to study

the streaks that maximize the disturbance growth over a specified streamwise interval. These studies provided useful recommendations based on theory. For example, Paredes et al. [8] demonstrated that the optimal streaks were most effective when the spanwise wavelength of the instability mode was equal to or smaller than twice the streak spacing. While these studies proved informative, the optimal growth theory does not tell how to generate optimal streaks. The optimal streaks may not even be physically realizable.

In a subsequent study, Paredes et al. [10] examined the effect of real vortex generators on a boundary layer at $M = 5.3$. These vortex generators were designed based on the insights from optimal growth theory. Transition analysis based on the e^n method indicated that the vortex generators could yield a transition delay of approximately 17%. Only three vortex generator geometries were studied, and hence, this study provided a limited exploration of the large space of possible parameters.

The important question for a researcher remains: How can one design a vortex generator that optimizes transition delay? In this study, a wider range of possible geometries is explored by using shape optimization techniques. By recasting the aerodynamic design process as a constrained optimal control problem [11, 12], the parameter space can be explored efficiently. At each iteration of the design optimization process, the search direction is informed by the gradient of the objective with respect to the shape parameters. Using the adjoint formulation, the computational cost of the gradient calculation is independent of the number of design parameters, and therefore an efficient optimization is enabled for a large number of design parameters. While this work does not cover all design parameters, the overall height, spanwise and streamwise extent, and shape of the vortex generator are considered. The focus of this paper is on methodology, tool development, and demonstration, rather than on presenting an optimal vortex generator geometry.

In Section II, the shape optimization process is presented. First, the mathematical formulation is introduced. This is followed by a discussion of the specific objective function and constraint imposed for this particular study. The specifics of the CFD solution and the gradient calculation are also introduced. In Section III, the geometry and flow conditions are outlined. Section III also includes a discussion of the numerical setup and the parameters used to discretely represent the vortex generator shape. Section IV presents the efforts to validate the numerical solution and verify the adjoint-based gradients Shape optimization results are presented in Section V, including qualitative and quantitative discussion of the optimized vortex generator shape.

II. Methods

A. Shape Design as an Optimization Problem

The basic formulation of the shape optimization is given as follows. The shape of the vortex generator is parameterized with a vector of design variables, α. The objective is to minimize some scalar function, J. The objective function, in general, depends on the flow field, U, which is computed on a discrete mesh denoted by a vector X. The flow field depends on the shape parameters, α, defining the geometry, i.e., $U = U(X(\alpha))$. For the cases considered here, the objective function depends on the design variables only indirectly, through the flow field $U(\alpha)$, i.e., $J = J(U(\alpha))$. The optimization problem is constrained by three conditions. First, the flow field must satisfy the compressible Navier-Stokes equations on the discrete grid. If R is the residual, then we require $R(U, X) = 0$. Second, the mesh must be deformed at each iteration depending on the design variables. To formally add this as a constraint, we denote the mesh deformation using a mapping from the design variables to the mesh $\mathcal{M} : \alpha \rightarrow X$. These two conditions can be expressed as:

$$R(U, X) = 0$$
$$\mathcal{M}(\alpha) = X$$

Third, a constraint is placed on the system to ensure that bypass transition does not occur. This constraint can be written as:

$$C(U) \geq 0 \tag{1}$$

The optimization problem can be written:

$$\min_{\alpha} \quad J(U) \tag{2}$$
$$\text{subject to} \quad R(U, X) = 0 \tag{3}$$
$$\mathcal{M}(\alpha) = X \tag{4}$$
$$C(U) \geq 0 \tag{5}$$

The Lagrangian associated with this problem is:

$$\mathcal{L}(\alpha, U, X, \bar{U}, \bar{X}, \bar{C}) = J(U) - R(U)^T \bar{U} - (\mathcal{M}(\alpha) - X)^T \bar{X} - C(U)^T \bar{C} \tag{6}$$

where $\bar{U}$, $\bar{X}$, and $\bar{C}$ are the Lagrange multipliers or adjoint variables. This is a general nonlinear programming problem, which can be solved iteratively using a sequential quadratic programming algorithm. SU2 uses the SciPy implementation [13] of Sequential Least SQuares Programming (SLSQP) [14]. SU2 and SLSQP will be discussed in more detail in Section II.C.

B. Objective Function and Constraint

The objective function in this study is based on the research into optimal streaks by Paredes et al. [6, 7]. This research established that streamwise streaks with suitable characteristics can be effective at damping the amplification of Mack modes in this flow. It was observed that the optimal streaks decayed very slowly in the streamwise direction. Therefore, to capture the cumulative effects of the streak over a long distance, the objective function is defined as an integral of the streak amplitude in the streamwise direction.

A useful measure to quantify the streak amplitude was developed by Fransson et al. [15]. They defined the streak amplitude as the largest variation of the streamwise velocity within a cross-section corresponding to a given streamwise location. This streak amplitude is a function of the streamwise coordinate, ξ, and can be expressed as:

$$A(\xi) = \frac{1}{2u_\infty} \max_{\eta} \left(\max_{\zeta}(u) - \min_{\zeta}(u) \right). \tag{7}$$

The empirical objective function to be minimized is defined as:

$$J = -\int_{\xi_1}^{\xi_2} A(\xi) \mathrm{d}\xi \tag{8}$$

where ξ_1 corresponds to a location just downstream of a vortex generator and ξ_2 corresponds to a fixed location far downstream. By convention, the optimization algorithm seeks a local minima of the objective, rather than a local maxima. This is why the objective is defined as the negative integral of the streak amplitude.

An increase in streak amplitude results in a decrease in the objective function. If the streak amplitude grows too large at any location, then bypass transition becomes more likely. Bypass transition can occur either due to the onset of self-sustained global modes or via overly strong streaks that lead to a rapid amplification of convective streak instabilities [8, 16]. For the optimal growth streaks examined by Paredes et al. [8], bypass transition occurred at $A \approx 0.25$. In other words, for the flow conditions of that particular study, the maximum spanwise variation in streamwise velocities should not exceed 25% of the freestream velocity. Due to differences in the maximum streak amplitude observed in fine- and coarse-grid simulations, the constraint in this study is placed at $A \approx 0.287$. This constraint is not necessarily general, and different values may be needed for other flow conditions. However, for simplicity, the same value is used for the limited purpose of demonstrating the shape optimization technique presented in this paper. This constraint can be expressed as:

$$\max_{\xi} \left(A(\xi) \right) \leq 0.287. \tag{9}$$

The objective function used here stands as a proxy for a full transition analysis, which would require a full direct numerical simulation (DNS) with stochastic forcing or, at the very least, a 2D PDE-based linear stability analysis. After optimization, the results should therefore be validated using such a stability analysis. Future work will be aimed at integrating the stability analysis into the shape optimization process, rather than leaving it as a post-processing step.

C. Shape Optimization in SU2

The Stanford University Unstructured (SU2) software suite [17, 18] was chosen as the driver for the shape optimization. SU2 integrates all of the steps needed for shape-optimization, including the forward solve, the discrete adjoint solve, the gradient calculation, and mesh deformation. These steps are depicted in the flowchart in Fig. 1. The first step is the forward solve, where the discretized Navier-Stokes equations are solved on the current mesh. The second step is the evaluation of the objective function, which is performed as a post-processing operation on the flow field. The shape optimization is typically run until improvements in the objective function fall below a user-specified threshold. If this criteria is met, then the optimizer stops. If it has not, then the optimizer finds a new set of shape parameters.

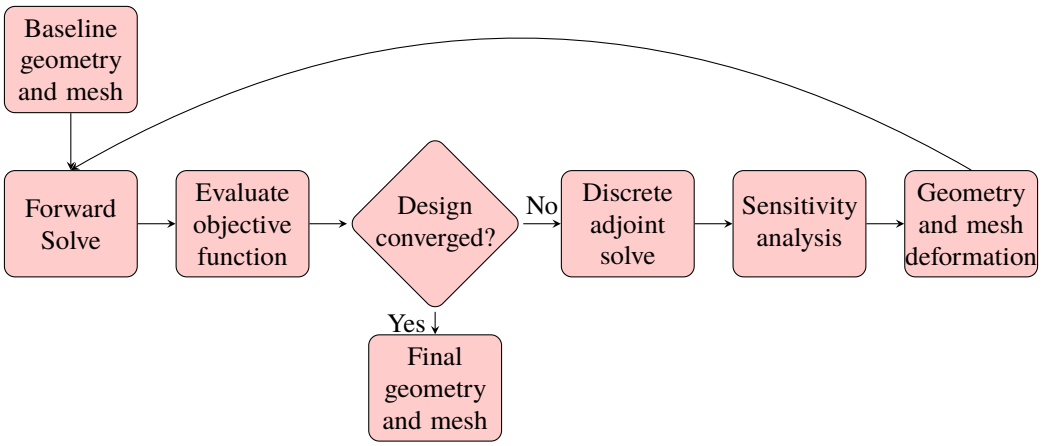

Fig. 1 Shape optimization process.

The discrete adjoint solver calculates the gradient of the flow field with respect to both the objective function and the maximum amplitude constraint. This gradient is projected onto the design space to calculate the sensitivity of the objective function with respect to the shape parameters. A new geometry and mesh are computed to match the shape parameters, and the whole process repeats until convergence.

From the perspective of shape optimization, a single "function evaluation" corresponds to deforming the grid, iterating the CFD solver till convergence, and post-processing the results. In this paper, the terms "function evaluation," "forward solve," and "direct solve" are used interchangeably.

The optimization loop is driven by the SciPy implementation [13] of Sequential Least SQuares Programming (SLSQP), which allows minimization of a scalar function of several variables under inequality and equality constraints. SLSQP is a local optimization algorithm that uses derivatives and an approximate Hessian to determine step size and direction at each design iteration. The SLSQP algorithm calls the corresponding parts of SU2 to complete each step. One shortcoming of the approach presented here is the use of a local optimization algorithm (e.g., SLSQP). This means that the results are not necessarily optimal in a global sense. While global optimization techniques are available, these techniques promote "exploration" of possibly bad solutions. Global optimization techniques therefore require a much greater number of function evaluations than local optimization techniques. For a CFD-based shape optimization, the cost of each function evaluation is relatively high. This makes global optimization prohibitively expensive for the present study.

SU2 solves the compressible Navier-Stokes equations using a finite volume method. The control volumes are constructed with a median-dual vertex-based scheme. The convective fluxes are calculated using the second-order central scheme with artificial dissipation by Jameson, Smith, and Turkel [19]. To calculate the viscous fluxes, flow quantities and their gradients are required at the faces of the control volumes. The gradients are calculated with a Green-Gauss method at all grid nodes. The flow quantities and their gradients are interpolated to the faces using a linear interpolation. For a uniform cubic grid and constant viscosity, this viscous flux calculation is equivalent to a second-order central-difference.

To solve the steady-state problem, pseudotime stepping is used with an implicit Euler scheme. Further details on the structure and numerics of SU2 can be found in its introductory papers [17, 18].

D. Discrete Adjoint

For the SLSQP algorithm, the gradients of both the objective function and the constraint are needed. The most straight-forward method of computing these gradients would be by perturbing the design variables and using finite difference formulas to obtain the gradients. However, the cost of this finite differencing step would scale linearly with the number of design variables, which can be quite large for shape optimization. Moreover, the appropriate choice of step size is not clear a priori. Therefore, a discrete-adjoint solver is used to compute the necessary gradients.

Full details of the discrete adjoint solver in SU2, including verification and validation, can be found in the papers by Albring et al. [20] and Economon et al. [21]. The discrete adjoint equations are constructed using algorithmic differentiation (AD). Using AD, the gradients of the flow and mesh equations, the objective function, and constraints as

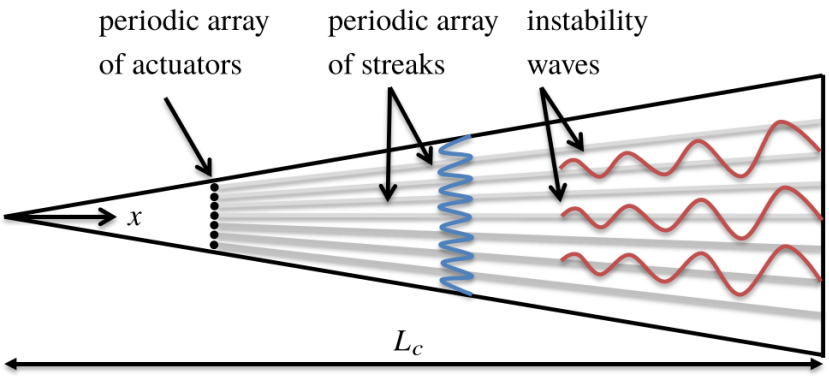

Fig. 2 A sketch of the cone used in the study. The computational domain only covers a slice of the full cone shown here.

well as the corresponding adjoint solutions are computed automatically, avoiding manual differentiation of discrete equations. This significantly reduces the difficulty and complexity of computing discrete adjoints for custom objectives and constraints.

III. Test Case

For this study, the boundary conditions and geometry were selected to match the $t^* = 21.5$s ascent phase of the HIFiRE-1 flight experiment, as described by Kimmel et al. [22] and Li et al. [23]. This configuration also matches the previous study and DNS by Paredes et al. [10]. The geometry is a 7° half-angle circular cone of length $L_c^* = 2.0$m. A sketch of the configuration is shown in Fig. 2. A laminar, axisymmetric boundary layer develops over the cone, with the freestream Mach number being $M_\infty = 5.3$. A row of vortex generators are inserted at $x^* = 0.603$m. These vortex generators are symmetrical and are arranged in pairs with equal but opposite orientations.

Two coordinate systems are used in this paper. The first is the global Cartesian coordinate system, with x aligned with the centerline of the cone and y and z perpendicular to the centerline. The second coordinate system is a local, body-fitted coordinate system. In this coordinate system, ξ is the "streamwise" direction, meaning that the coordinate direction ξ is parallel to the cone wall and perpendicular to the azimuthal direction. The wall normal direction is denoted η and the azimuthal direction is denoted ζ.

For all the parameters described in this paper, the freestream values of velocity, density, temperature, and viscosity are used for nondimensionalization. Dimensional quantities are marked with an asterisk, e.g., L^*. For the lengthscale, a reference of $L^* = 1.0$m is used. Where relevant, lengths are also nondimensionalized by a boundary layer thickness δ_h^*. This second length-scale is only used where explicitly stated. The boundary-layer thickness is defined as the wall-normal position where the total enthalpy reaches 99.5% of its freestream value. The reference value of $\delta_h^* = 8.708 \times 10^{-4}$m is measured at the vortex generator location in the absence of the vortex generators (i.e., for an unperturbed axisymmetric boundary layer).

A. Numerical Setup

To reduce the computational complexity, the computational domain was limited along the azimuthal direction to include a single pair of vortex generators, rather than a full ring around the cone. The azimuthal extent of the domain is 1.125° instead of the full 360°. The inflow plane is located at $\xi = 0.452$, or approximately $172\delta_h$ upstream of the vortex generators. The outflow plane is located at $\xi = 2.15$. The wall-normal extent of the domain is a linear function of the ξ coordinate, starting with $\eta = 0.0404$ at $\xi = 0.452$ and ending with $\eta = 0.192$ at the outlet.

Periodic boundary conditions are imposed in the azimuthal direction. An isothermal, no-slip viscous wall boundary condition is used for the cone surface. The temperature at the wall is set to $T^* = 397$K. While the experiment and corresponding DNS had spatially-varying wall temperatures, the variation in temperature across the length of the axial domain is less than 2%. Supersonic outflow conditions are specified at the outflow plane. The nose region of the cone was also excluded from the computational domain. Supersonic inflow conditions corresponding to specified spatially-varying flow quantities are imposed along the inflow plane and the farfield. These values are extracted from the

Table 1 Grid resolutions used in this study. The DNS from [10] used higher-order numerics in addition to the increased resolution. The $\Delta\eta_w^+$ listed is the wall-normal grid spacing of the first point, measured just before the vortex generators at the axial position $\xi = 0.600$.

	N_ξ	N_η	N_ζ	$\Delta\eta_w^+$
DNS [10]	983	257	192	0.6
Fine	983	257	192	0.6
Medium	491	128	96	1.2
Coarse	245	64	48	2.4

DNS results by Paredes et al. [10]. While the DNS imposed a sponge layer at the farfield boundary to prevent reflections of outgoing waves, no sponge layer was used in this computation.

Various grid resolutions are used in this study. Shape optimization requires many forward solves, totaling more than 30 in the present study. For the major iterations of the optimizer, i.e., excluding line search iterations, each forward solve is coupled with two discrete adjoint computations. For this reason, using the DNS resolution and DNS numerics for every single adjoint solve is prohibitively expensive. Consequently, the coarse grid was used for shape optimization. The grid details, including the grid size in viscous units, are listed in Table 1. The grids were derived from the DNS grid used in Paredes et al. [10]. The fine grid was the same as the DNS grid. The coarser grids were designed by removing 1/2 or 3/4 of the points along each direction. For comparison, the DNS of Paredes et al. [10] used a sixth-order accurate spatial scheme, instead of the second-order spatial numerics used in SU2.

A constant CFL number of 10 was used for pseudotime steps, and a localized underrelaxation scheme was used to step through the initial transients. The discrete-adjoint solution depends on the solution of the forward problem. Inaccuracies in the forward solve can lead to inaccuracies or failure to converge in the discrete-adjoint solve. For this reason, the forward solve was converged to a higher precision than the adjoint solve. The forward solve was run until the density residual decreased by about 7 orders of magnitude, compared with the initial residuals for uniform freestream values. The adjoint solver was run until the adjoint density residual decreased by about 5 orders of magnitude, for both the integral objective and the maximum amplitude constraint.

B. Shape Parameters

The surface shape in the region of the vortex generators is parameterized using a free-form deformation (FFD). To control the FFD, two boxes are used with 17x2x13 nodes in the streamwise, wall-normal, and spanwise directions, respectively. One box is placed over each vortex generator, and the deformations are constrained to be symmetric. The size of the FFD used here can be compared to the size of the baseline geometry, In this discussion and the rest of this paper, the “baseline geometry” is the single row of vortex generators examined in Ref. [10]. The baseline vortex generators extend between approximately $\xi = 0.603$ and $\xi = 0.607$, whereas the FFD box covers the axial interval of $\xi = 0.600$ and $\xi = 0.608$. This allowed the vortex generator to extend further in the upstream, downstream, and azimuthal directions as it was optimized. The spanwise spacing of the vortex generators is based on the results from the studies of optimal streaks [7, 8] and the previous vortex generator study by Paredes et al. [10]. This spacing was left fixed and was not part of the design variables.

Second-order uniform B-splines are used to create surface deformations from the FFD box. This choice is consistent with the second-order accuracy of the spatial numerics. Two possibilities existed for applying the shape deformation. The first was to use the baseline geometry as a starting point and deform that shape. With this option, zero deformation would imply that the baseline geometry would be maintained. The total height of the vortex generator would be the addition of the height of the baseline geometry and the deformation. Unfortunately, it is complicated to limit the total height to be positive using this option. Vortex generators are usually added to a surface, rather than subtracted from it. For this reason, the design space was limited to positive total heights and the first option was not used. In that context, a recent study examined the effect of negative surface deformations on the streak characteristics behind a patch of distributed surface roughness by suppressing the "dimples" within an otherwise smooth height distribution, and the streak characteristics with and without the negative deformations were approximately similar [24].

The second option, which was used in this study, is to define the vortex generator itself as a surface deformation. With this option, zero deformation implies a smooth cone surface and no vortex generator. The total height of the

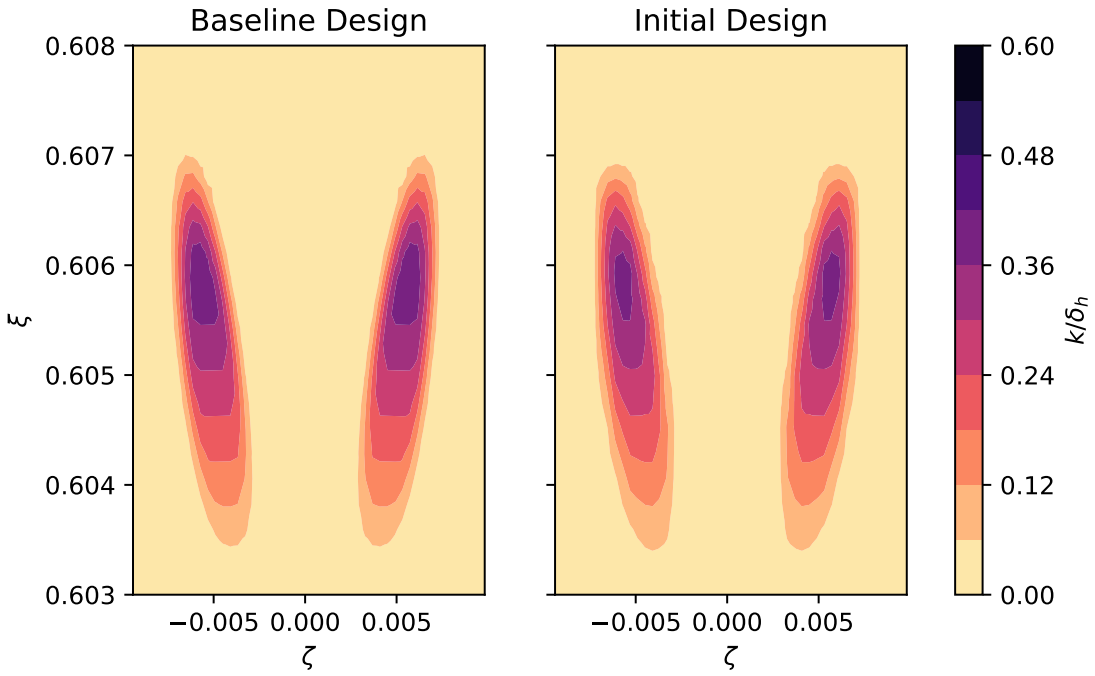

Fig. 3 A comparison of the baseline vortex generator shape and the initial vortex generator shape. While some differences are present, the average relative difference in height perturbation over all the surface mesh points with a nonzero deformation was only 3.3%.

vortex generator is the height of the deformation, and a positive-only limit on the total height is easy to enforce. One disadvantage of this option is that the baseline geometry cannot be exactly represented with the FFD described here. The shape optimization was instead initialized with the closest possible B-spline representation. Contour plots of the baseline and initial vortex generators can be seen in Fig. 3. The average relative difference in the height perturbation over all the surface mesh points with a nonzero deformation was 3.3%. The mismatch was largest where sharp changes occurred in the baseline shape, due to the smooth nature of the B-splines and the limited number of FFD nodes in these regions.

As seen in Section V, the initial shape is sufficiently different from the baseline geometry that the resulting streak amplitudes are significantly lower than a well-resolved parameterization of the vortex generators. These differences indicate that the limited number of FFD nodes and the B-spline representation limit the space of possible surface deformations. Nevertheless, the results presented in Section V establish that these limitations do not prevent the algorithm from yielding significant improvements over the baseline geometry.

To ensure second-order continuity in the streamwise and spanwise directions, the boundary nodes of the combined FFD domain in those two directions are not used as design variables. Specifically, the two outer planes on each spanwise side are fixed, and a single outer plane on each streamwise side is fixed. The FFD box in the right half of the domain is shown in Fig. 4. The wall-normal positions of the FFD nodes are used as the design variables. The maximum wall-normal deformation of the surface with respect to a smooth cone was constrained to be less than $k/\delta_h < 0.574$. For reference, the baseline vortex generators had a maximum height of $k/\delta_h \approx 0.4$. A maximum wall-normal deformation of $k/\delta_h \leq 1.0$ was initially tested in order to allow vortex generators to cross the whole boundary layer. In practice, none of the initial tests resulted in a surface deformation greater than $k/\delta_h > 0.52$. The value of 0.574 was selected as a more suitable bound for the design space. As will be seen in the results (Sec. V), this bound did not limit the final, optimized geometry.

While the full domain included two FFD boxes, these boxes were not deformed independently. At each iteration, the surface deformations were forced to be symmetric. This limitation was imposed in order to match the previous studies on symmetric vortex generators and symmetric streaks.

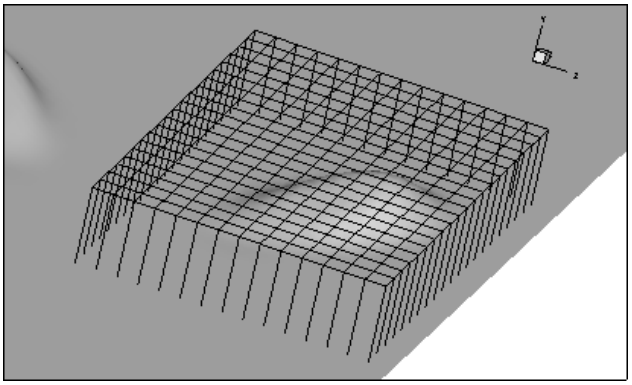

Fig. 4 FFD box for a single vortex generator. Two symmetric FFD boxes are used, one over each vortex generator. The vortex generators displayed in this figure correspond to the baseline geometry. The boundary nodes of the FFD box in the spanwise and streamwise directions were not used as design variables.

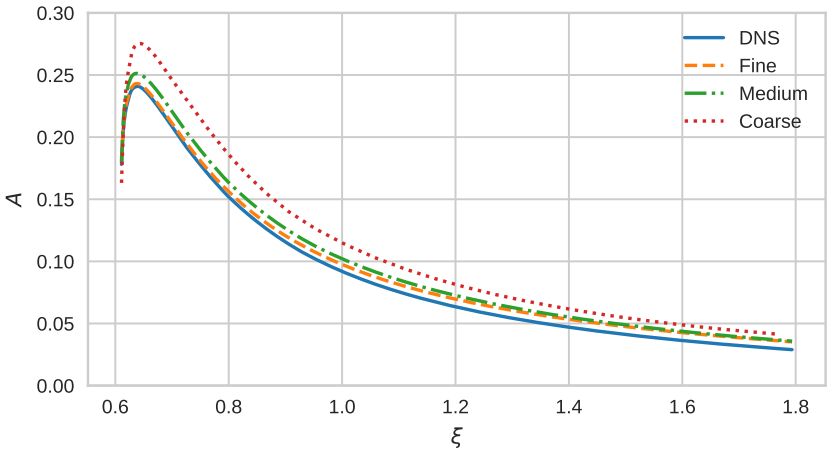

Fig. 5 Comparison of the streak amplitude between the selected resolutions in SU2 and the fine resolution, high-order DNS.

IV. Verification and Validation

A. Forward Solve

For validation purposes, a forward solve in SU2 was compared with the DNS data previously published by Paredes et al. [10]. The goal here is twofold. First, the convergence of SU2 to the DNS data is presented, to provide confidence in SU2's forward or direct solve. Second, the qualitative features of the solution are examined on the coarse-grid solutions. The streak amplitude, $A(\xi)$, given in Eq. 7, is a local measure of how effective the vortex generator is at creating streamwise streaks. Since the streak amplitude is directly relevant to the control of instability amplification, it is used as the basis for comparing the accuracy of different grids. The results are plotted in Fig. 5. As expected, the coarse resolution provides only a somewhat crude approximation to the actual streak amplitude. Following the systematic refinement of the mesh, the solution appears to converge to the DNS solution, especially just downstream of the vortex generators. The streak amplitudes far downstream are still slightly overpredicted, even on the fine grid. The difference in spatial numerics or the lack of a farfield sponge layer are both possible explanations for this discrepancy. Nevertheless, this difference amounts to less than 3% of the maximum streak amplitude. The qualitative features of the boundary layer deformation due to the vortex generators are captured sufficiently, as described in the following paragraphs.

For a comparison of the overall structure of the disturbances, the crossplane velocity contours are shown in Fig. 6 for several streamwise positions. The streak amplitude is directly related to the magnitude of the "crests" and "valleys" seen in the contour plots: a stronger disturbance will have larger crests and valleys. While there are differences in the height

of the crests further downstream, especially at $\xi = 0.90$, the overall structure of the disturbances is very similar at all levels of resolution examined.

Shape optimization requires many more computations than a single forward run, and there is a trade-off between computational feasibility and solution accuracy. Even though the coarse SU2 solutions are inadequate to capture the effect of the vortex generators on the Mack Mode amplification in the absolute sense, the authors believe that the methodology presented here provides a reasonable framework to assess the relative effect of the different vortex generator geometries. This is especially true for this initial stage of tool prototyping and development. For these reasons, the coarse grid was used for the shape optimization process.

B. Verification of Discrete Adjoint

As part of the shape optimization, a new objective function (Eq. 8) and constraint (Eq. 9) have been added to SU2. In order to verify the gradients obtained using the discrete adjoint, the numerical values of those gradients were compared to the gradients obtained from a simple finite differencing operation. In this verification test, a reduced set of one design variable was used.

The gradients were computed for both the objective function, Eq. 8, and the maximum amplitude constraint. Gradients of the lift and the drag coefficients were also calculated to provide a reference for the expected accuracy. These gradients for lift and drag have been previously verified by the developers of SU2 [20, 21]. A comparison of the gradients computed via both methods (namely, discrete adjoints and finite differences) is displayed in Fig. 7 for all four functions: the drag coefficient, the lift coefficient, the objective function, and the constraint. Shown in the figure is the relative difference between the two gradient computations, i.e.,

$$\varepsilon(J) = \left(\left(\frac{\partial J}{\partial \alpha} \right)_{FD} - \left(\frac{\partial J}{\partial \alpha} \right)_{DA} \right) \Bigg/ \left(\frac{\partial J}{\partial \alpha} \right)_{DA} . \tag{10}$$

As the step size in the finite differencing becomes smaller, the differences between the finite difference gradient and the discrete adjoint gradient reduce to less than 1%. Differences between the two gradients are not expected to converge to zero, since the finite-differencing method becomes unreliable when the finite-difference step size is much smaller than the grid size.

V. Results

As mentioned in the previous sections, the "baseline design" corresponds to the single row of vortex generators examined in Paredes et al. [10]. Since the baseline design could not be exactly represented with a B-spline parameterization over the selected FFD nodes, the shape optimization was initialized with the closest possible B-spline representation. Because of this, the initial value of the objective function was only 60% of the baseline value, and the maximum streak amplitude was also lower. Despite this suboptimal starting point, the shape-optimization process successfully decreased the objective function without violating the constraints. In terms of this specific problem, this means that the final design has an increased integral of the streak amplitude, while the maximum streak amplitude did not exceed the imposed limits.

The progression of both the integral of the streak amplitude and the maximum streak amplitude can be seen in Fig. 8. The value of the objective function is expressed as a ratio with respect to the baseline geometry, i.e., a value of $J/J_b = 1$ means no change. Since J is always negative, minimizing J is equivalent to maximizing the ratio J/J_b. As previously noted, the objective function started with smaller absolute values, but doubled to obtain a value 20.3% larger than the baseline value. This improvement was accomplished in 13 outer optimization iterations and 30 function evaluations, including the line-search iterations.

While the objective and constraints are scalar measures, the improvements in the streak amplitude can also be verified by examining the streak amplitude as a function of the streamwise coordinate, ξ. The baseline and final streak amplitudes are plotted in Fig. 9. A significant increase in streak amplitude can be seen over most of the streamwise direction. At $\xi = 1.0$, the steak amplitude is 25.9% larger. This plot in Fig. 9 also provides a visual confirmation that the maximum streak amplitude is nearly identical to the baseline value.

Several significant differences can be seen in a visual inspection of the geometry. The shape of the final vortex generator design is shown as a contour plot in Fig. 10 and with a perspective view in Fig. 11. The maximum height increased by 33%. This maximum height of $k/\delta_h < 0.512$ falls below the FFD limit of $k/\delta_h < 0.574$, meaning that this limit on the shape parameters did not affect the final design. The optimized geometry was constrained by the maximum streak amplitude, rather than arbitrary limits on the design space.

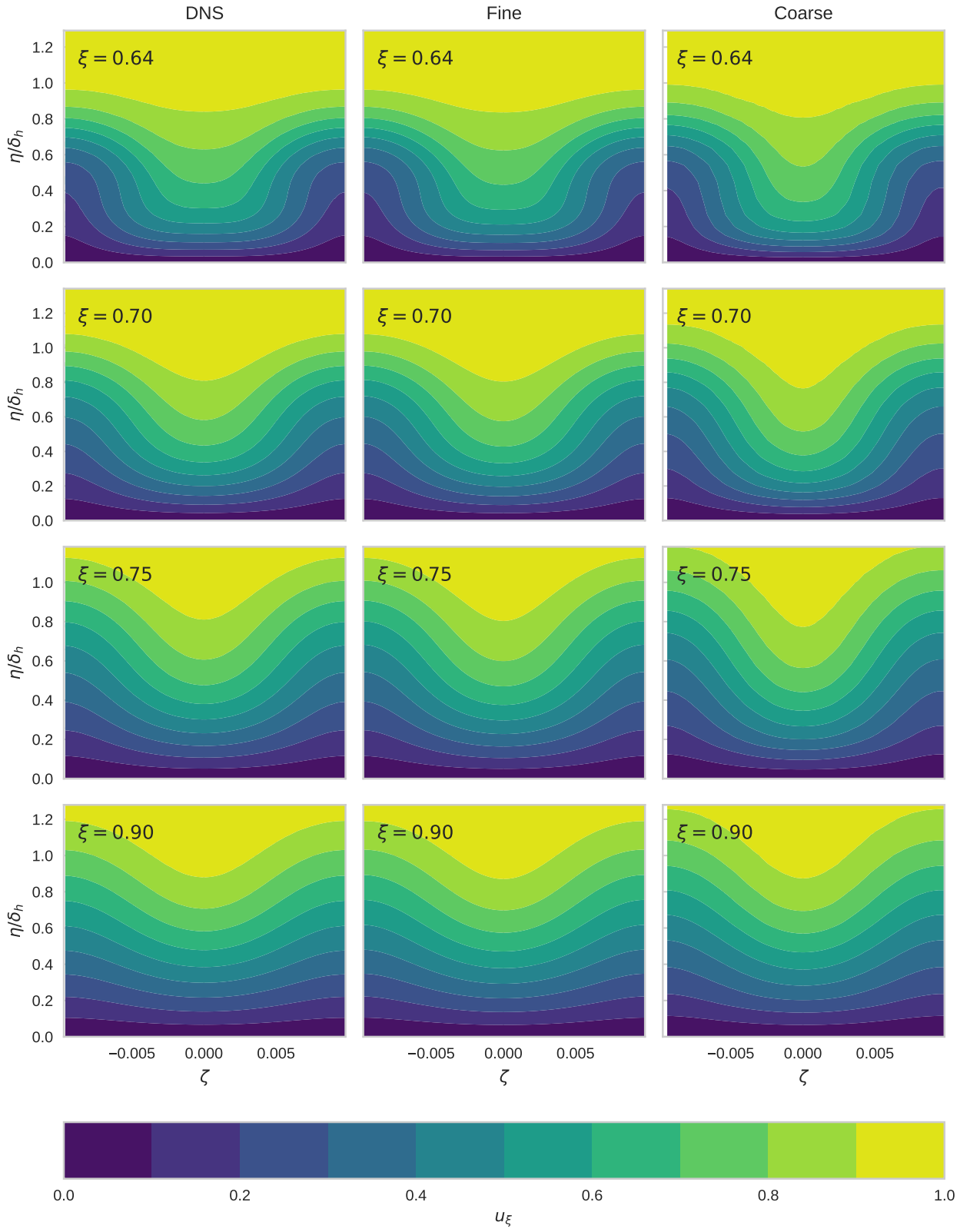

Fig. 6 **Crossplane contours of the streamwise velocity, u_ξ, in various crossplanes. The first position, at $\xi = 0.64$, is the approximate location of the maximum streak amplitude in the reference DNS.**

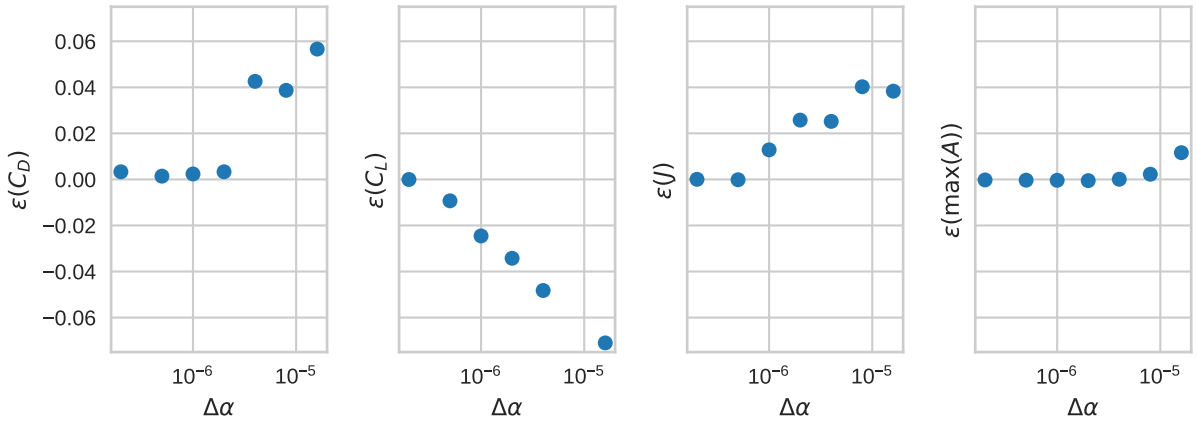

Fig. 7 Relative difference (ε) between gradients computed with finite differencing and the discrete adjoint, as a function of finite difference step size. The gradients are calculated with respect to the shape deformation parameter, α. Shown is the relative difference for the lift coefficient, drag coefficient, the empirical objective function, and the maximum streak amplitude.

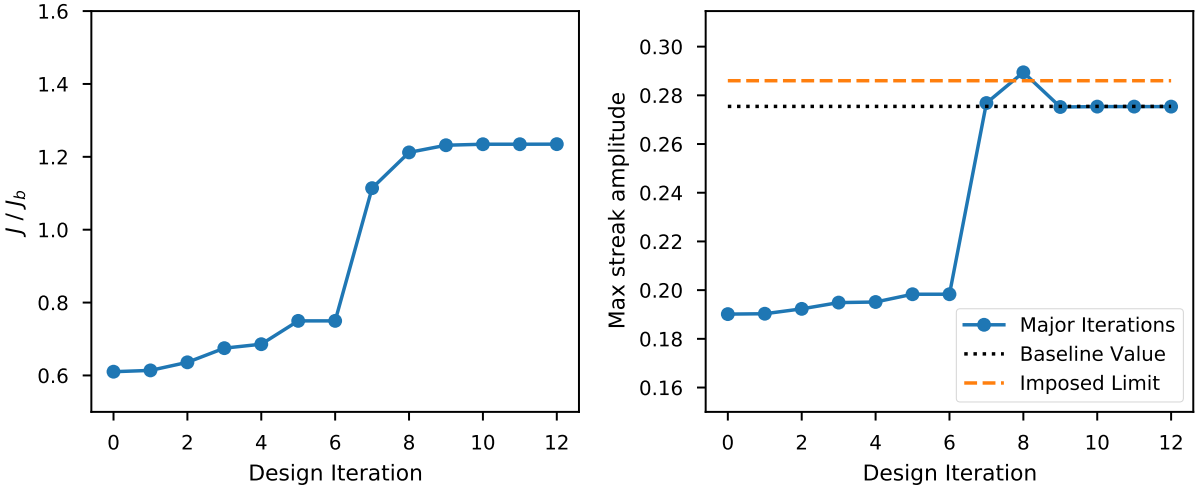

Fig. 8 Change in the objective function and the constraint during the shape optimization process. The objective function here is the integral of the streak amplitude, as defined in Eq. 8. The value of the objective function is expressed as a ratio with respect to the baseline geometry, i.e., a value of $J/J_b = 1$ means no improvement. The major iterations shown here are the outer iterations of the optimization, and do not include the line-search iterations.

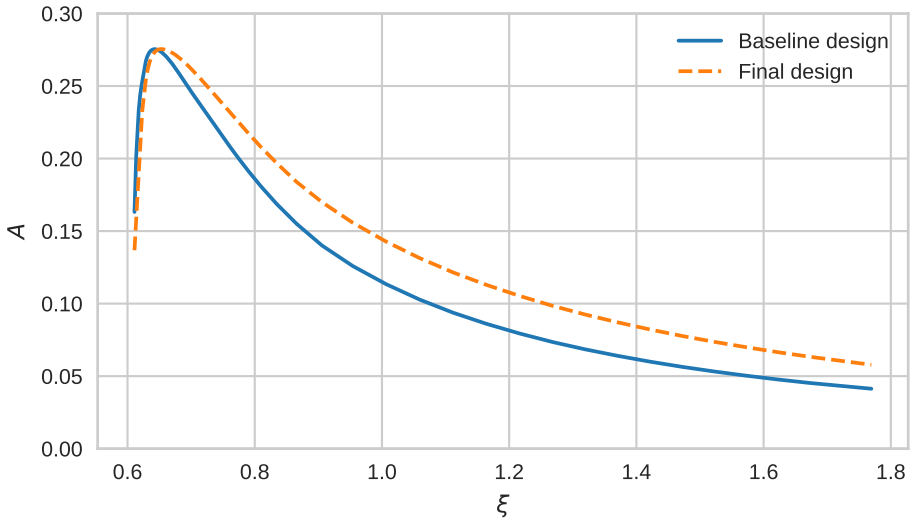

Fig. 9 Streak amplitude as a function of the streamwise distance, for both the baseline and final designs.

The optimized vortex generator also extends further in both the downstream and azimuthal directions. While the vortex generators were free to grow in the upstream direction, the upstream edge remained relatively fixed. Most noticeable is the transformation from an elliptic bump to an epsilon shape. The sharp improvement seen in the optimization history (see Fig. 8) occurred when this epsilon shape was established. In a previous study, Paredes et al. [10] found that two alternating rows of vortex generators, facing in opposing directions, were more effective at delaying transition than a single row of vortex generators. The optimized geometry seems to possess a similar zigzag shape, but contained within a single row.

VI. Conclusions and Future Work

This paper presents a new approach for the design of vortex generators that are intended to reduce the amplification of Mack mode instabilities in hypersonic boundary layers. The design process is cast as a constrained shape optimization problem, where the objective is to maximize the integral of the streak amplitude while imposing an upper bound on the streak amplitude. The upper bound is imposed to avoid a premature onset of transition due to overly strong streaks. This approach relies on algorithmic differentiation (AD) to obtain the sensitivity of the objective and constraints with respect to the design variables. This AD framework and the accompanying discrete adjoint solver are implemented in SU2, a suite of open-source software tools.

The conditions of the demonstration correspond to a hypersonic flow around an axisymmetric body. The test case matches the $t^* = 21.5$s trajectory point during the ascent phase of the HIFiRE-1 flight experiment. For validation, the SU2 solutions computed on coarse, medium, and fine meshes were compared to previously published DNS data. The streak amplitude evolution based on the SU2 solutions indicated a progressively closer agreement with the DNS prediction as the computational grid was refined toward the DNS grid. An objective function and constraint, specific to measuring the axial evolution of the streak amplitude behind the vortex generators, were added to SU2. The gradients of the objective and constraint were calculated using discrete adjoints, and these gradients were verified by comparison with the gradients calculated using finite differences.

The shape-optimization technique is applied to a pair of vortex generators within a Mach 5.3 axisymmetric boundary layer. The value of the objective function improved by 20.3%, and the streak amplitude was increased over most of the domain downstream of the vortex generators. This was achieved without exceeding the maximum allowed streak amplitude. The optimized vortex generators also displayed a distinct epsilon shape that differed significantly from the baseline geometry.

These initial results, based on optimization on a relatively coarse grid, demonstrate the potential for new insights to be gained from an adjoint-based design of vortex generators. The shape-optimization process is capable of answering

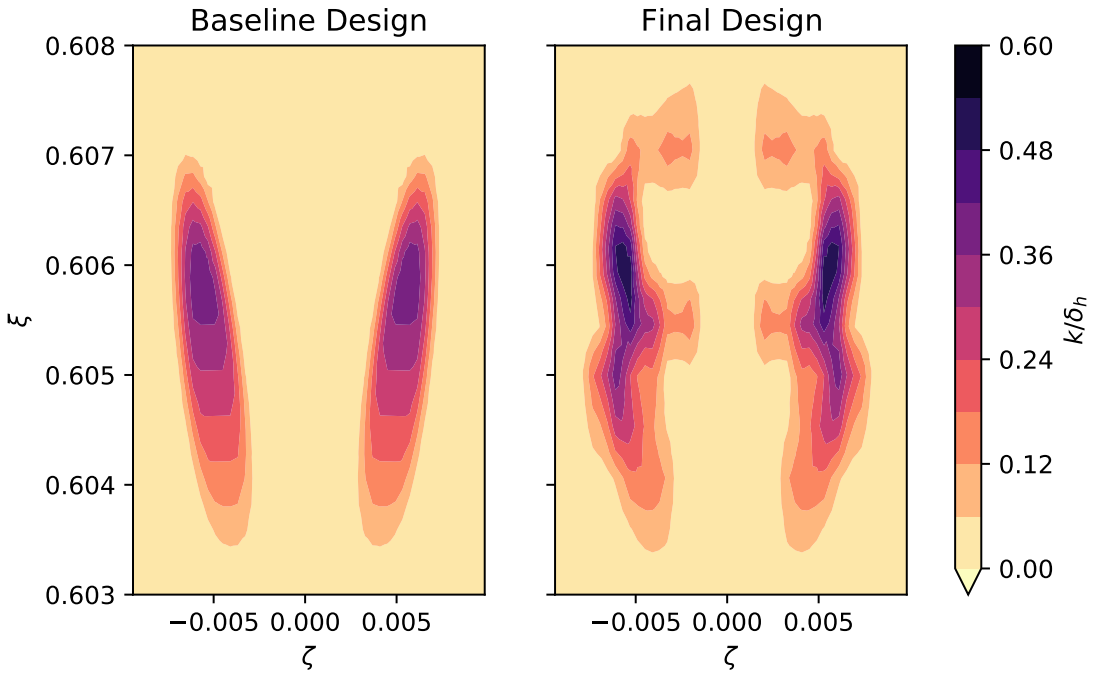

Fig. 10 Contour plots of the normalized roughness element height, k/δ_h, as measured from the cone wall.

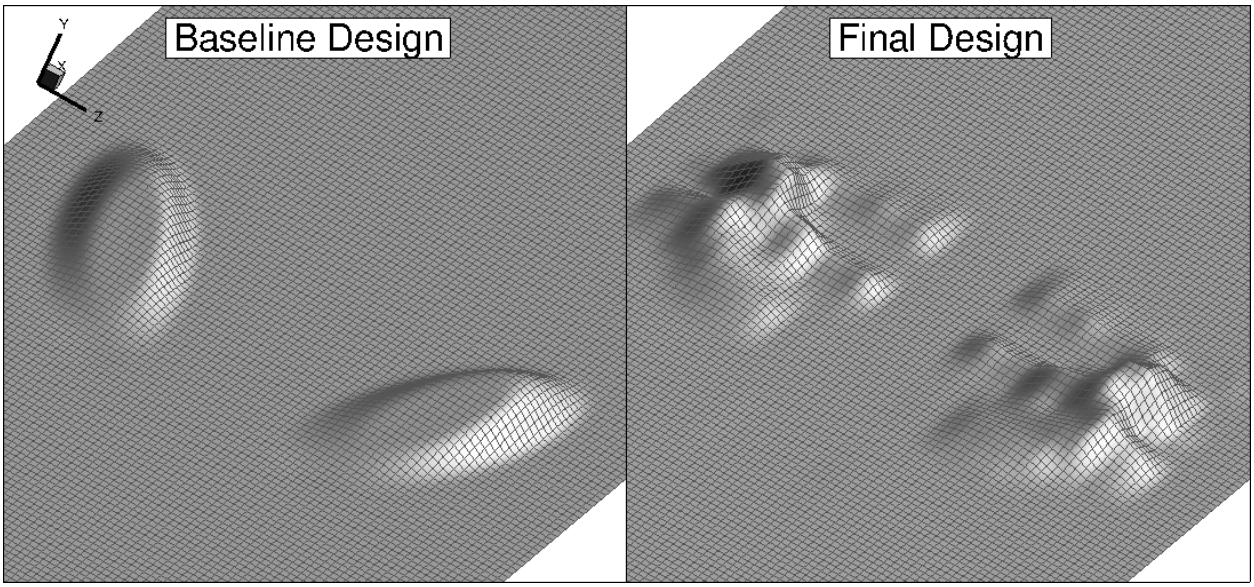

Fig. 11 Perspective view of the baseline and final vortex generator shapes. Because the pair of vortex generators cover a narrow $1.125°$ azimuthal extent, the z scale has been magnified 5 times with respect to the x and y scales.

questions like "How tall should the vortex generators be?" or "How far should the vortex generator extend in the streamwise direction?" Moreover, the relatively intuitive baseline shape in this study evolved into a more elaborate geometry. This is one of the powerful capabilities of adjoint-based shape optimization: researchers can start with simple vortex generators, based on theory, and then optimize these shapes into complex, high-performing designs.

In the near future, the computed solution for the final vortex generator will be verified using the fine mesh. Besides confirming the gain in the objective function, the fine mesh computations can rule out the possibility of an absolute instability in the nearfield due to the increase in the maximum height of the vortex generator, relative to the baseline geometry. The fine mesh solution will then be used as the basic state for formal stability analysis similar to that in Ref. [10], yielding a comparison between the instability amplification over the baseline and optimized vortex generator designs. This will be used to verify the expectation that the final design causes later transition to turbulence and to quantify that delay.

Several possibilities exist to extend this work even further. Since a local optimization was performed with a nonconvex objective function, the optimized geometry is not necessarily a global optimum. A global optimization algorithm could be used to promote further exploration of the vortex generator design space. Given enough computational resources, an algorithm such as simulated annealing or basin hopping will likely produce better results. Multiple starting geometries could also be used as a brute-force approach to global optimization. The empirical objective function here could also be refined to a more complex transition analysis. The discrete adjoint framework in SU2 makes such a change in the objective function relatively easy.

This shape optimization methodology could also be applied to multiple rows of vortex generators. Two successive rows of vortex generators were studied by Paredes et al. [10], and found to be more effective than a single row. Adding multiple stages of vortex generators rapidly increases the number of parameters that must be studied. Since the computational cost of the discrete adjoint solve is independent of the number of design variables, the methodology presented here allows multiple stages to be optimized together, while keeping the computational cost low.

Acknowledgments

This work was supported by the NASA Langley Research Center. MC would like to acknowledge support from the Transformational Tools and Technologies Project. Computational resources for this research were provided by the NASA High-End Computing (HEC) Program through the NASA Advanced Supercomputing (NAS) Division at Ames Research Center. This material is based upon work supported by the National Science Foundation Graduate Research Fellowship under Grant No. 1610403.

References

[1] Mack, L. M., "Boundary Layer Linear Stability Theory," *Agard*, Vol. Report 709, No. 709, 1984, pp. 1–81.

[2] James, C. S., "Boundary-Layer Transition on Hollow Cylinders in Supersonic Free Flight as Affected by Mach Number and a Screwthread Type of Surface Roughness," Tech. rep., NASA Ames Research Center, Moffett Feld, CA, 1959.

[3] Fong, K. D., Wang, X., and Zhong, X., "Numerical Simulation of Roughness Effect on the Stability of a Hypersonic Boundary Layer," *Computers & Fluids*, Vol. 96, 2014, pp. 350–367.

[4] Fong, K. D., Wang, X., Huang, Y., Zhong, X., McKiernan, G. R., Fisher, R. A., and Schneider, S. P., "Second Mode Suppression in Hypersonic Boundary Layer by Roughness: Design and Experiments," *AIAA Journal*, Vol. 53, No. 10, 2015, pp. 3138–3144.

[5] Paredes, P., "Advances in Global Instability Computations: From Incompressible To Hypersonic Flow," Ph.D. thesis, Universidad Politécnica de Madrid, March 2014.

[6] Paredes, P., Choudhari, M. M., and Li, F., "Transition Delay in Hypersonic Boundary Layers via Optimal Perturbations," Tech. Rep. NASA/TM-2016-219210, NASA Langley Research Center, Hampton, Virginia, 2016.

[7] Paredes, P., Choudhari, M. M., and Li, F., "Instability Wave-Streak Interactions in a High Mach Number Boundary Layer at Flight Conditions," *Journal of Fluid Mechanics*, Vol. 858, 2019, pp. 474–499. https://doi.org/10.1017/jfm.2018.744.

[8] Paredes, P., Choudhari, M. M., and Li, F., "Instability Wave–Streak Interactions in a Supersonic Boundary Layer," *Journal of Fluid Mechanics*, Vol. 831, 2017, pp. 524–553. https://doi.org/10.1017/jfm.2017.630.

[9] Holloway, P. F., and Sterrett, J. R., "Effect of Controlled Surface Roughness on Boundary-Layer Transition and Heat Transfer at Mach Numbers of 4.8 and 6.0," Tech. Rep. NASA TN D-2054, NASA Langley Research Center, Hampton, Virginia, 1964.

[10] Paredes, P., Choudhari, M. M., and Li, F., "Transition Delay via Vortex Generators in a Hypersonic Boundary Layer at Flight Conditions," *AIAA Aviation Forum*, Atlanta, Georgia, 2018, pp. 1–13. https://doi.org/10.2514/6.2018-3217.

[11] Pironneau, O., "On Optimum Design in Fluid Mechanics," *Journal of Fluid Mechanics*, Vol. 64, No. 1, 1974, pp. 97–110. https://doi.org/https://doi.org/10.1017/S0022112074002023.

[12] Jameson, A., "Aerodynamic Design via Control Theory," Tech. Rep. ICASE Report No. 88-64, NASA Langley Research Center, Hampton, Virginia, 1988.

[13] Jones, E., Oliphant, T., and Peterson, P., "Scipy: Open Source Scientific Tools for Python," , 2001. URL http://www.scipy.org/.

[14] Kraft, D., "A Software Package for Sequential Quadratic Programming," Tech. Rep. Tech. Rep. DFVLR-FB 88-28, DLR German Aerospace Center – Institute for Flight Mechanics, Koln, Germany, 1988.

[15] Fransson, J. H., Brandt, L., Talamelli, A., and Cossu, C., "Experimental and Theoretical Investigation of the Nonmodal Growth of Steady Streaks in a Flat Plate Boundary Layer," *Physics of Fluids*, Vol. 16, No. 10, 2004, pp. 3627–3638. https://doi.org/10.1063/1.1773493.

[16] Choudhari, M., Li, F., Wu, M., Chang, C. L., Edwards, J., Kegerise, M., and King, R., "Laminar-Turbulent Transition Behind Discrete Roughness Elements in a High-Speed Boundary Layer," *48th AIAA Aerospace Sciences Meeting Including the New Horizons Forum and Aerospace Exposition*, 2010, pp. 1–21. https://doi.org/10.2514/6.2010-1575.

[17] Palacios, F., Alonso, J., Duraisamy, K., Colonno, M., Hicken, J., Aranake, A., Campos, A., Copeland, S., Economon, T., Lonkar, A., Lukaczyk, T., and Taylor, T., "Stanford University Unstructured (SU2): An Open-Source Integrated Computational Environment for Multi-Physics Simulation and Design," *51st AIAA Aerospace Sciences Meeting*, 2013, pp. 1–60. https://doi.org/10.2514/6.2013-287.

[18] Palacios, F., Economon, T. D., Aranake, A., Copeland, S. R., Lonkar, A. K., Lukaczyk, T. W., Manosalvas, D. E., Naik, K. R., Padron, S., Tracey, B., Variyar, A., and Alonso, J. J., "Stanford University Unstructured (SU2): Analysis and Design Technology for Turbulent Flows," *52nd Aerospace Sciences Meeting*, Vol. 51, 2014, pp. 1–19. https://doi.org/10.2514/6.2014-0243.

[19] Jameson, A., Schmidt, W., and Turkel, E., "Numerical Solutions of the Euler Equations by Finite Volume Methods Using Runge-Kutta Time-Stepping Schemes," *AIAA paper*, 1981. https://doi.org/10.2514/6.1981-1259.

[20] Albring, T. A., Sagebaum, M., and Gauger, N. R., "Development of a Consistent Discrete Adjoint Solver in an Evolving Aerodynamic Design Framework," *AIAA Aviation Forum*, 2015. https://doi.org/10.2514/6.2015-3240.

[21] Economon, T. D., Alonso, J. J., Albring, T. A., and Gauger, N. R., "Adjoint Formulation Investigations of Benchmark Aerodynamic Design Cases in SU2," *AIAA Aviation Forum*, 2017. https://doi.org/10.2514/6.2017-4363.

[22] Kimmel, R. L., Adamczak, D., Paull, A., Paull, R., Shannon, J., Pietsch, R., Frost, M., and Alesi, H., "HIFiRE-1 Ascent-Phase Boundary-Layer Transition," *Journal of Spacecraft and Rockets*, Vol. 52, No. 1, 2015, pp. 217–230. https://doi.org/10.2514/1.A32851.

[23] Li, F., Choudhari, M., Chang, C. L., Kimmel, R., Adamczak, D., and Smith, M., "Transition Analysis for the Ascent Phase of HIFiRE-1 Flight Experiment," *Journal of Spacecraft and Rockets*, Vol. 52, No. 5, 2015, pp. 1283–1293. https://doi.org/10.2514/1.A33258.

[24] Choudhari, M. M., Li, F., and Paredes, P., "Effect of Distributed Patch of Smooth Roughness Elements on Transition in a High-Speed Boundary Layer," *AIAA 2018 Fluid Dynamics Conference*, AIAA 2018-3532, Atlanta, GA, 2018. https://doi.org/10.2514/6.2018-3532.